LETTERS
PUBLISHED ONLINE: 24 FEBRUARY 2013 | DOI: 10.1038/NPHOTON.2013.13

nature photonics

# Detecting single infrared photons with 93% system efficiency

F. Marsili[1]*, V. B. Verma[1], J. A. Stern[2], S. Harrington[1], A. E. Lita[1], T. Gerrits[1], I. Vayshenker[1], B. Baek[1], M. D. Shaw[2], R. P. Mirin[1] and S. W. Nam[1]*

**Single-photon detectors[1] at near-infrared wavelengths with high system detection efficiency (>90%), low dark count rate (<1 c.p.s.), low timing jitter (<100 ps) and short reset time (<100 ns) would enable landmark experiments in a variety of fields[2–6]. Although some of the existing approaches to single-photon detection fulfil one or two of the above specifications[1], to date, no detector has met all of the specifications simultaneously. Here, we report on a fibre-coupled single-photon detection system that uses superconducting nanowire single-photon detectors[7] and closely approaches the ideal performance of single-photon detectors. Our detector system has a system detection efficiency (including optical coupling losses) greater than 90% in the wavelength range $\lambda = 1{,}520$–$1{,}610$ nm, with a device dark count rate (measured with the device shielded from any background radiation) of $\sim$1 c.p.s., timing jitter of $\sim$150 ps full-width at half-maximum (FWHM) and reset time of 40 ns.**

Superconducting nanowire single-photon detectors (SNSPDs)[7,8] have outperformed other near-infrared single-photon detector technologies in terms of dark count rate, timing resolution and reset time[1]. However, after over ten years of research, the system detection efficiency (SDE, which includes the efficiency of the optical coupling to the detector) of SNSPDs has been limited to 36% at a wavelength $\lambda$ of 1,550 nm (ref. 9) because (i) the superconducting material used (typically, polycrystalline NbN) has limited compatibility with the structures that enhance the optical coupling and absorption of the detectors, and (ii) the internal detection efficiency (the probability that the absorption of one photon in a nanowire results in a response pulse) of typical SNSPDs (based on 100-nm-wide NbN nanowires) does not show saturation as a function of the bias current $I_B$. The superconducting properties of NbN films depend on the crystal phase of the films[10] and are affected by crystal defects[11], which limits (i) the fabrication yield of large-area devices[12], (ii) the choice of substrates for fabrication and (iii) the design parameters of optical structures that would enhance absorption in the nanowires. Furthermore, although 30- and 20-nm-wide NbN nanowires have demonstrated saturated detection efficiency at $\lambda = 1{,}550$ nm (ref. 13), the fabrication of large-area SNSPDs (which allow efficient optical coupling) based on such narrow nanowires remains challenging. We recently reported on the fabrication of SNSPDs based on a different superconducting material, amorphous tungsten silicide ($W_{0.75}Si_{0.25}$, or WSi)[14]. Because the crystal structure of WSi is homogeneously disordered, WSi superconducting nanowires are more robust with respect to structural defects than NbN nanowires (which allows the fabrication of larger-area devices), can be deposited on a variety of substrates, and allow more degrees of freedom in optimizing the optical coupling and the absorption of the detectors. Furthermore, WSi SNSPDs based on nanowires as wide as 150 nm have shown saturated SDE versus $I_B$ curves[14] in the near-infrared, probably because the size of the photon-induced perturbation of the superconducting

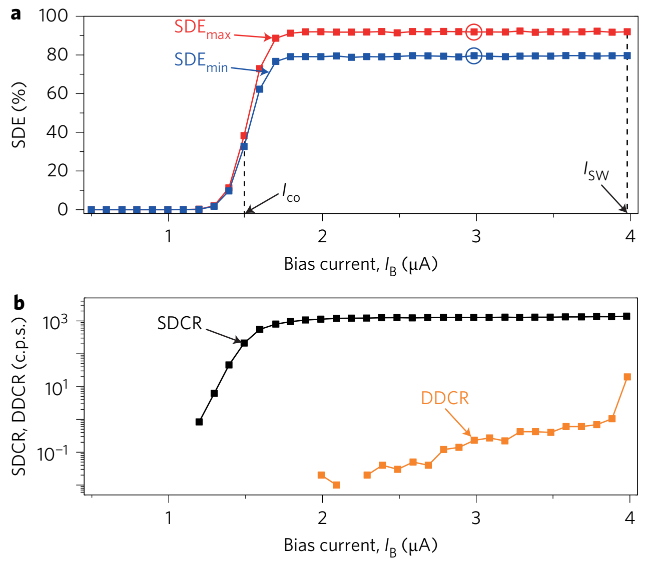


**Figure 1 | Bias current dependence of SDE, SDCR and DDCR. a**, SDE versus bias current $I_B$ for two different polarizations of light at $\lambda = 1{,}550$ nm. The SNSPD used was based on 4.5-nm-thick, 120-nm-wide nanowires with a pitch of 200 nm. The SNSPD covered a square area with dimensions of 15 μm × 15 μm. The dashed lines indicate the cutoff current ($I_{co}$, which is defined as the bias current at the inflection point of the SDE versus $I_B$ curve[13]) and the switching current ($I_{SW}$, which is defined as the maximum current the device could be biased at without switching to the normal, non-superconducting state) of the device. At $I_B = 3$ μA, the average and 1σ uncertainty of the maximum and minimum SDE were $SDE_{max} = 93.2 \pm 0.4$% (red circle) and $SDE_{min} = 80.5 \pm 0.4$% (blue circle) (Supplementary sections 'Estimation of the system detection efficiency', 'Estimation of the uncertainty on the system detection efficiency'). The experimental value of the SDE was lower than the design value of the absorption of the SNSPDs (>99%), which we attribute to several possible causes (Supplementary sections 'Optical simulations of the system detection efficiency', 'Refractive indexes of the materials employed in the optical stack'): (i) our imperfect knowledge of the refractive index of the materials used in the optical stack; (ii) fabrication imperfections; (iii) coupling losses; and (iv) the non-unity internal detection efficiency of the SNSPDs. **b**, SDCR and DDCR versus $I_B$ for the device in **a**. The $SDE_{max}$, $SDE_{min}$ and SDCR curves were obtained at $T = 120$ mK by averaging six subsequent acquisitions of the curves. Error bars for each point are not plotted for clarity, but the uncertainty is described in Supplementary section 'Estimation of the uncertainty on the system detection efficiency'.

[1]National Institute of Standards and Technology, 325 Broadway, MC 815.04, Boulder, Colorado 80305, USA, [2]Jet Propulsion Laboratory, California Institute of Technology, 4800 Oak Grove Drive, Pasadena, California 91109, USA. *e-mail: francesco.marsili@nist.gov; saewoo.nam@nist.gov

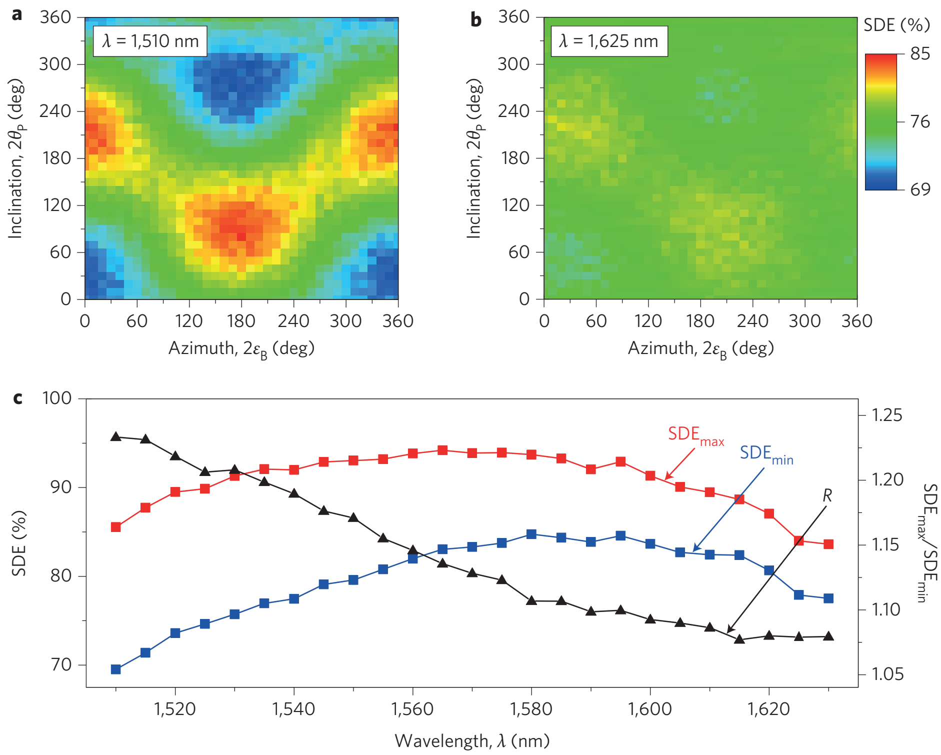


**Figure 2 | Polarization and wavelength dependence of SDE. a,b**, SDE (in colour scale) versus the inclination ($2\theta_P$) and azimuth ($2\varepsilon_B$) angles of the polarization vector on the Poincaré sphere at $\lambda = 1{,}510$ nm (**a**) and $\lambda = 1{,}625$ nm (**b**). The ratio between maximum and minimum values of the SDE ($R = \mathrm{SDE}_{max}/\mathrm{SDE}_{min}$) varied from $R = 1.23$ at $\lambda = 1{,}510$ nm to $R = 1.08$ at $\lambda = 1{,}625$ nm because the wavelength dependence of the absorption of the optical stack was different for different polarizations[23,24] (Supplementary section 'Optical simulations of the system detection efficiency'). **c**, Wavelength dependence of maximum SDE ($\mathrm{SDE}_{max}$), minimum SDE ($\mathrm{SDE}_{min}$) and ratio $R = \mathrm{SDE}_{max}/\mathrm{SDE}_{min}$. The measured parameters of the optical stack are, from top (illumination side) to bottom, 213-nm-thick $TiO_2$, 231-nm-thick $SiO_2$, 4.5-nm-thick, 120-nm-wide WSi nanowires with 200 nm pitch, 230-nm-thick $SiO_2$, 80-nm-thick gold. The thickness of the WSi layer was estimated from the deposition time. The thicknesses of the $TiO_2$ and $SiO_2$, layers were estimated by white-light ellipsometry on reference samples from the deposition runs. The width and pitch of the nanowires were measured by scanning electron microscopy. Experimental $\mathrm{SDE}_{max}$ versus $\lambda$ and $\mathrm{SDE}_{min}$ versus $\lambda$ curves were obtained by averaging three subsequent acquisitions. The bias current was $I_B = 3.8$ μA and the temperature was $T = 120$ mK.

state[15,16] is larger in WSi than in NbN. In earlier reported work[14], WSi SNSPDs only achieved SDE ≈ 20% at $\lambda = 1{,}550$ nm because the detectors were fabricated on bare oxidized silicon wafers and were manually aligned to the optical fibre. Here, we report WSi SNSPDs embedded in an optical stack designed to enhance absorption (Supplementary section 'Fabrication') at $\lambda = 1{,}550$ nm and coupled to single-mode optical fibres at $\lambda = 1{,}550$ nm with a self-aligned mounting scheme based on silicon micromachining[17]. Using WSi SNSPDs, we constructed a detector system with SDE as high as ~93% around $\lambda = 1{,}550$ nm, a system dark count rate of ~$1 \times 10^3$ c.p.s. (primarily due to background radiation), a timing jitter of ~150 ps full-width at half-maximum (FWHM) and a reset time of 40 ns. The only other single-photon detector that has demonstrated SDE > 90% at $\lambda = 1{,}550$ nm is the transition-edge sensor (TES)[18]. However, the TES has orders of magnitude larger recovery time (~1 μs) and timing jitter (the best value to date is ~5 ns; ref. 19) than WSi SNSPDs, and requires a complicated superconducting readout circuit.

We characterized our single-photon detection system by using 28 different SNSPDs from five fabrication runs. We measured SDE > 85% with 50% of the detectors tested so far (Supplementary section 'List of characterized devices'). Figure 1a shows the bias dependence of SDE (Methods and Supplementary section 'Estimation of the system detection efficiency') for our best device. As the detection efficiency of SNSPDs varies with the polarization of the incident light[20], the polarization state of the light was varied on the Poincaré sphere to maximize or minimize the counts from the detector. We therefore obtained a maximum ($\mathrm{SDE}_{max}$, red curve) and minimum ($\mathrm{SDE}_{min}$, blue curve) SDE versus $I_B$ curve. Both the $\mathrm{SDE}_{max}$ and $\mathrm{SDE}_{min}$ curves had a sigmoidal shape, and saturated at $\mathrm{SDE}_{max} \approx 93\%$ and $\mathrm{SDE}_{min} \approx 80\%$ for $I_B$ values larger than a cutoff current $I_{co} = 1.5$ μA and lower than the switching current of the device, $I_{SW} = 4$ μA. Figure 1b shows the bias dependence of the system dark count rate (SDCR, the response pulse count rate measured when the input fibre to the system is blocked by a shutter) and of the device dark count rate (DDCR, the response pulse count rate measured when the fibre is disconnected from the device inside the refrigerator). The SDCR versus $I_B$ curve has a sigmoidal shape similar to the SDE versus $I_B$ curves shown in Fig. 1a, and saturated at SDCR ≈ $1 \times 10^3$ c.p.s. for $I_B > I_{co}$. The DDCR was ≤1 c.p.s. for most of the bias range ($I_B \leq 0.97 I_{SW}$), which is approximately two orders of magnitude lower than the DDCR of NbN SNSPDs with a similar active area and fill factor[21]. We concluded that the SDCR is dominated by background photons.

Typically, the detection efficiency of SNSPDs varies significantly with the polarization of the incident light (by a factor of ~2 at $\lambda = 1{,}550$; refs 20,22). However, a detector with polarization-insensitive SDE would be desirable for many applications[1]. We therefore characterized the polarization and wavelength dependence of the SDE by mapping the SDE onto the Poincaré sphere in the wavelength range $\lambda = 1{,}510$–$1{,}630$ nm (we call these plots Poincaré maps of the SDE). Figure 2a,b shows the Poincaré maps at $\lambda = 1{,}510$ nm and $\lambda = 1{,}625$ nm. The positions of the maxima and minima of the Poincaré maps are approximately the same at

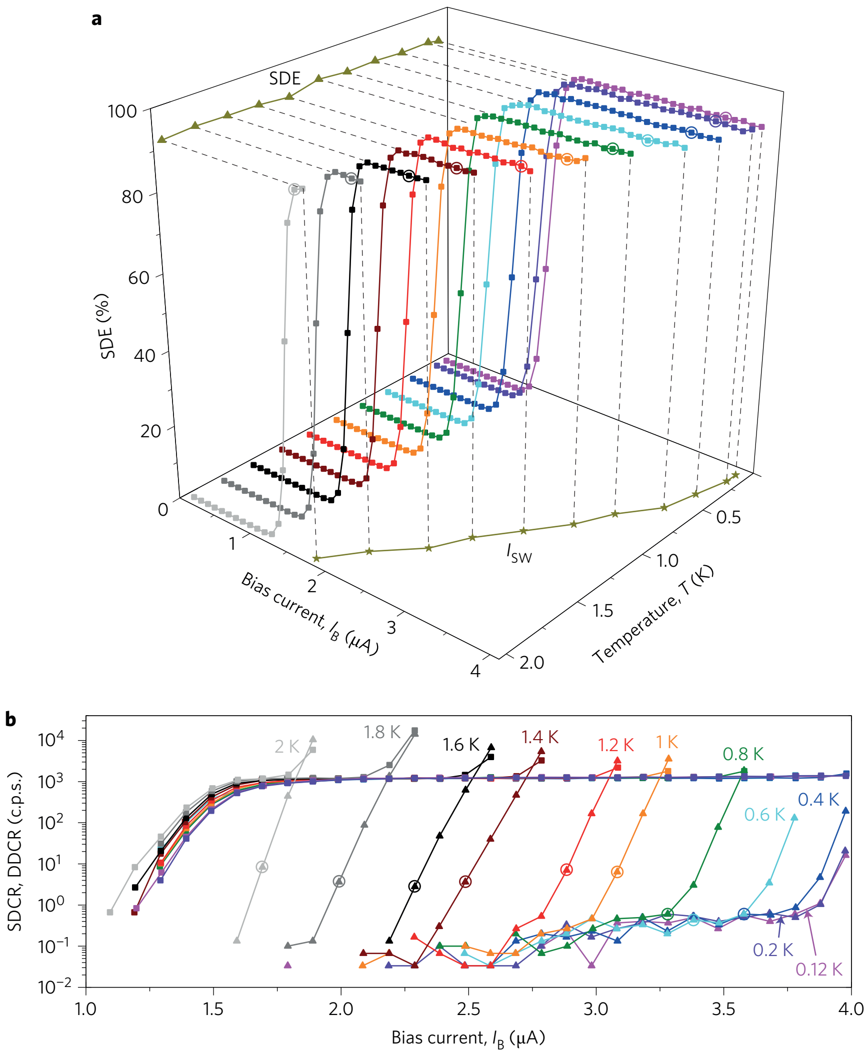


**Figure 3 | Temperature dependence of SDE, SDCR and DDCR. a**, SDE at $\lambda = 1{,}550$ nm versus bias current $I_B$ and temperature $T$. Dark yellow curves on the $I_B$–$T$ and SDE–$T$ planes represent the temperature dependence of $I_{SW}$ (stars) and SDE at $I_B = I_{SW}$ (triangles). Coloured circles indicate the data point at which $I_B \approx 0.9 I_{SW}$ and SDE $\approx$ 90% at each temperature. **b**, SDCR (squares) and DDCR (triangles) versus bias current $I_B$ in the temperature range $T = 0.12$–2 K. Coloured circles indicate the data point at which $I_B \approx 0.9 I_{SW}$ and DDCR < 10 c.p.s. at each temperature (the circles for $T = 0.4$, 0.2 and 0.12 K overlap). SDCR and DDCR curves were obtained by averaging three consecutive acquisitions of the curves. We did not observe any variation in $I_{SW}$ between the different acquisitions of the curves.

the two wavelengths. However, the ratio between maximum and minimum values of the SDE ($R = \mathrm{SDE}_{max}/\mathrm{SDE}_{min}$) change with wavelength. Figure 2c shows the wavelength dependence of $\mathrm{SDE}_{max}$ (red squares), $\mathrm{SDE}_{min}$ (blue squares) and $R$ (black triangles), which were obtained by extracting the maxima and minima of the Poincaré maps at each wavelength. Although the SDE of our detector showed a non-negligible polarization dependence, the results shown in Fig. 2c suggest that the optical stack could be designed to eliminate the polarization dependence of the SDE at a particular wavelength (which, however, may differ from the wavelength for the maximum SDE).

Most of the readily accessible closed-cycle refrigeration technologies[25] do not reach a base temperature below 1 K. It would therefore be desirable to operate our detector above 1 K without degrading its performance. As the critical temperature of our SNSPD was $T_C = 3.7$ K, we characterized the performance of the system as a function of temperature by measuring the bias dependence of SDE, SDCR and DDCR in the temperature range $T = 120$ mK–2 K. As shown in Fig. 3a, although $I_{SW}$ decreases and approaches $I_{co}$ with increasing temperature (dark yellow stars on the $I_B$–$T$ plane), the SDE versus $I_B$ curve saturates to ~93% over the whole temperature range $T = 120$ mK–2 K (dark yellow triangles on the SDE–$T$ plane). As shown in Fig. 3b, the DDCR at the switching current increases with temperature, from ~20 c.p.s. at $T = 120$ mK to ~$10 \times 10^3$ c.p.s. at $T = 2$ K, and is comparable to the SDCR for $T > 0.8$ K. Although the bias range for efficient, low-dark-count-rate single-photon detection decreases with increasing temperature, the detector shows SDE $\approx$ 90% and DDCR < 10 c.p.s. for $I_B \approx 0.9 I_{SW}$ over the temperature range investigated (coloured circles in Fig. 3a,b), confirming that we could operate the detector system at relatively high cryogenic temperature without significantly degrading its sensitivity.

We characterized the timing performance of the detector system by measuring the histogram of the inter-arrival time[13,26] of the response pulses and the timing jitter at $T = 120$ mK. Although in conventional NbN SNSPDs the decay time of the response pulse has been traditionally used as an estimate of the reset time of the detector[27], in our detector the reset time is significantly shorter than the decay time. As shown in Fig. 4a, the decay time of the response pulse of the SNSPD ($\tau$) is $\tau \approx 120$ ns. However, Fig. 4b

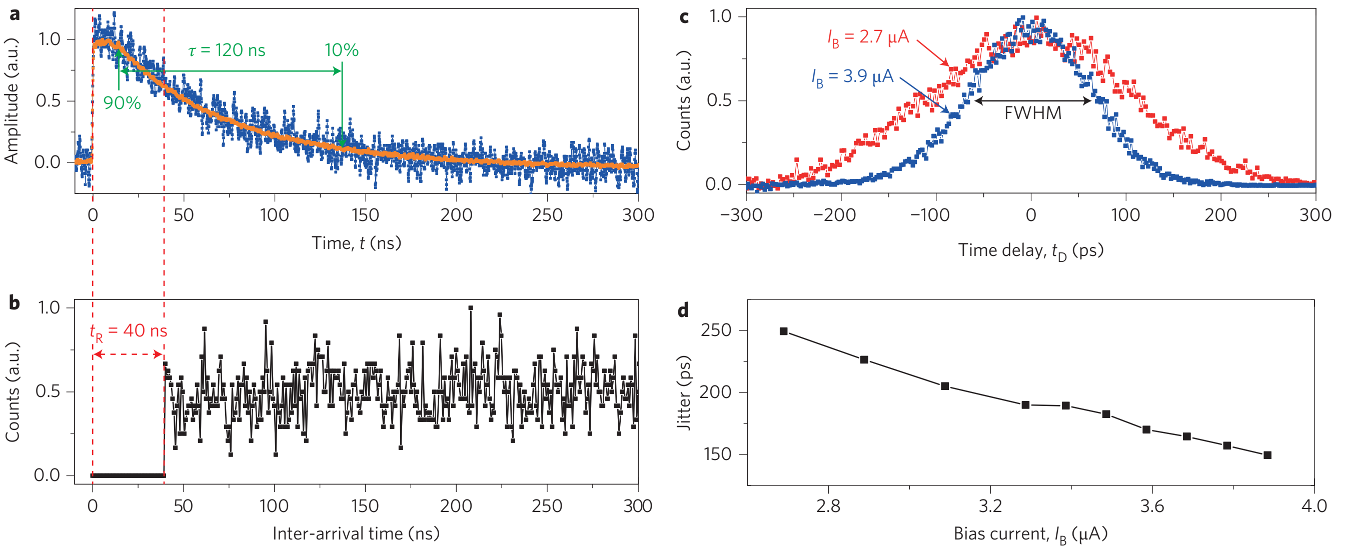


**Figure 4 | Reset time and jitter. a,** Single-shot (blue curve) and averaged (orange curve) oscilloscope traces of the response pulse of the SNSPD biased at $I_B = 3.8$ μA ($I_B = 0.95 I_{SW}$). The time $t$ at which the curves reach 50% of the maximum of the average trace (158 mV) with positive slope was set to $t = 0$ s. The curves were normalized by the maximum of the average trace. The decay time of the SNSPD ($\tau$) was defined as the time required for the pulse to decay from 90% to 10% of the maximum of the pulse (green arrows). **b**, Histogram of inter-arrival time (the period between two consecutive response pulses when the SNSPD is illuminated with a continuous-wave laser) of the SNSPD biased at $I_B = 3.8$ μA ($I_B = 0.95 I_{SW}$). The reset time ($t_R$) is defined as the period required for the histogram of the inter-arrival time to reach the first non-zero value. The histogram was normalized by its maximum value. **c**, IRF of the SNSPD biased at $I_B = 3.9$ (blue curve) and $I_B = 2.7$ μA (red curve). The IRF at a particular $I_B$ was obtained by calculating the histogram of the time delay $t_D$ between the rising edge of the synchronization pulse of the laser and the rising edge of the response pulse of the SNSPD. Each IRF was normalized by its maximum value. The black arrow indicates the FWHM of the IRF acquired at $I_B = 3.9$ μA. **d**, Current dependence of the jitter of the detector system.

shows that the reset time of the detector ($t_R$) is as low as $t_R = 40$ ns. The fact that $t_R$ is a factor of ~3 lower than $\tau$ is due to the low $I_{co}$ of the detector ($I_{co} \approx 0.4 I_{SW}$; see Fig. 1a). Indeed, when the SNSPD switched back to the superconducting state after a hot spot nucleation event, it was sufficient that the current in the nanowire increased above ~$0.4 I_{SW}$ for the SDE to recover fully. Figure 4c shows the instrument response function (IRF) of the detector system illuminated with a femtosecond-pulse laser for two different bias currents. The IRF becomes broader with decreasing $I_B$. Figure 4d shows the current dependence of the jitter of the detector system, which we define as the FWHM of the IRF. The system jitter decreases from 250 ps at $I_B = 0.67 I_{SW}$ to 150 ps at $I_B = 0.97 I_{SW}$. As the jitter increases with decreasing $I_B$ and $I_{SW}$ decreases with increasing temperature, operating the detector at higher temperature would result in a degradation of its timing resolution. The jitter of our detector system is higher than the values of 30–50 ps typically reported for conventional NbN SNSPDs[8]. However, the system jitter is dominated by the electrical noise of the readout circuit, rather than the intrinsic jitter of WSi SNSPDs (Supplementary section 'Noise contribution to the jitter').

In conclusion, our single-photon detector system based on WSi SNSPDs demonstrated SDE ≈ 90% at $\lambda = 1{,}550$ nm and DDCR < 10 c.p.s. up to a temperature of $T = 2$ K. We expect our detector system to achieve a system dark count rate limited by the device intrinsic dark count rate (SDCR ≈ DDCR < 1 c.p.s.) by improving the filtering of the background photons. In the future, by adopting a parallel architecture (superconducting nanowire avalanche photodetector, SNAP[13,28,29]), we expect to reduce the reset time of our SNSPDs to <10 ns and to increase the signal-to-noise ratio[13], which would allow the jitter of the detector system to be reduced. Finally, because of the relatively large bias range with saturated detection efficiency at $\lambda = 1{,}550$ nm, WSi SNSPDs have the potential for high fabrication yield across a silicon wafer and broad wavelength sensitivity[14,30]. These two features will enable two major advancements in the near future: (i) high SDE in the mid-infrared wavelength range, and (ii) large SNSPD arrays with near-unity efficiency from the visible to the mid-infrared spectral regions.

## Methods

**Detector system and measurement set-up.** The experimental set-up used for the optical characterization of our detector system is presented in Supplementary section 'Measurement set-up'. For the SDE and inter-arrival time measurements, we illuminated the detector using a fibre-coupled continuous-wave tunable laser with tuning range $\lambda = 1{,}510$–$1{,}630$ nm. For jitter measurements, we used a mode-locked fibre laser with emission around 1,560 nm, pulse width of <100 fs and repetition rate of ~35 MHz. We controlled the polarization of the light from the lasers with a polarization controller. The light was then coupled to three variable optical attenuators (with nominal attenuation $A_1$, $A_2$ and $A_3$) and to a micro-electro-mechanical system optical switch. The optical switch diverted the light at its input to the detector system (we call this output the detector port) or to a calibrated (Supplementary section 'Calibration of the optical power meters') InGaAs optical power meter (we call this output the control port).

After fabrication, a device could be removed from the wafer[17] and mounted inside a zirconia sleeve with an optical fibre. Holding both the detector chip and the optical fibre, the zirconia sleeve realized an optical alignment with a typical accuracy of ±3 μm (ref. 17). All of the optical fibres used were silica C-band single-mode fibres. The optical fibre coupled to the detector inside the cryostat (a cryogen-free adiabatic demagnetization refrigerator) was coated with a multi-dielectric-layer anti-reflection coating that reduced the reflectivity $\rho$ at the interface between the silica and the air (or vacuum) below 0.3% in the wavelength range of interest. The fibre coupled to the detector was then spliced to a fibre inside the cryostat. That cryostat fibre was fed out of the cryostat through a vacuum feed-through and then spliced to a fibre coupled to the detector port of the optical switch.

The detectors were wire-bonded to launching pads connected to brass coaxial cables (2 GHz electrical bandwidth at 300 K). The devices were current-biased with a low-noise voltage source in series with a 10 kΩ resistor through the d.c. port of a room-temperature bias-tee (40 dB isolation, 100 kHz–4.2 GHz bandwidth on the radiofrequency port). The readout circuit consisted of a chain of two low-noise, room-temperature amplifiers (100 kHz–500 MHz bandwidth, 24 dB gain, 2.9 dB noise figure) connected to the radiofrequency port of the bias-tee. The amplified signal was connected to a 225 MHz bandwidth counter (for detection efficiency measurements) or to an 8 GHz bandwidth, 20 Gsample/s oscilloscope (for jitter and inter-arrival time measurements).

**Estimation of SDE.** The SDE was measured as the ratio of the photoresponse count rate (PCR) and the number of photons in the SNSPD fibre ($N_{ph}$), where SDE = PCR/$N_{ph}$. PCR was estimated as the difference between the response-pulse count rate (CR), measured with the laser beam attenuated ~80 dB ($A_2 = A_3 =$ 40 dB) and coupled to the detector, and the SDCR. We defined the SDCR as the response pulse count rate measured with the laser beam blocked by the shutters of the variable optical attenuators. $N_{ph}$ at a particular wavelength $\lambda$ was calculated by using an estimate of the optical power in the SNSPD fibre ($P_{SNSPD}$) and the energy of a single photon at that wavelength.

The SDE was measured at a particular wavelength with the following procedure. (i) We measured the splitting ratio of the optical switch ($R_{SW}$), which we defined as the ratio between the power at the detector and control ports of the switch. (ii) We then measured the real attenuation of attenuator 2,3 ($\alpha_{2,3}$) when the nominal attenuation of attenuator 2,3 was set to 40 dB ($A_1 = A_{3,2} = 0$ dB and $A_{2,3} = 40$ dB). (iii) With the attenuation of attenuator 2,3 set to zero ($A_2 = A_3 = 0$ dB), we varied the attenuation of attenuator 1 ($A_1$) to obtain the desired input optical power in the control port ($P_C$). (iv) We then closed the shutters of the three attenuators and measured the SDCR versus $I_B$ curve. (v) We opened the shutters of the three attenuators, set the attenuation of attenuator 2 and 3 to 40 dB ($A_2 = A_3 = 40$ dB) to reduce the optical power to the single-photon level (~$50 \times 10^3$ photons per second), and measured the CR versus $I_B$ curve. We calculated the optical power in the SNSPD fibre as $P_{SNSPD} = P_C \cdot \alpha_2 \cdot \alpha_3 \cdot R_{SW}/(1 - \rho)$. Further details are presented in Supplementary sections 'Estimation of the system detection efficiency', 'Estimation of the uncertainty on the system detection efficiency', 'Stability of the optical'.

Received 2 August 2012; accepted 9 January 2013; published online 24 February 2013

## References

1. Eisaman, M. D., Fan, J., Migdall, A. & Polyakov, S. V. Invited Review Article: Single-photon sources and detectors. *Rev. Sci. Instrum.* **82,** 071101 (2011).
2. Garg, A. & Mermin, N. D. Detector inefficiencies in the Einstein–Podolsky–Rosen experiment. *Phys. Rev. D* **35,** 3831–3835 (1987).
3. Ladd, T. D. *et al.* Quantum computers. *Nature* **464,** 45–53 (2010).
4. Gisin, N. & Thew, R. Quantum communication. *Nature Photon.* **1,** 165–171 (2007).
5. Li, D. D. U. *et al.* Video-rate fluorescence lifetime imaging camera with CMOS single-photon avalanche diode arrays and high-speed imaging algorithm. *J. Biomed. Opt.* **16,** 096012 (2011).
6. Weibring, P., Edner, H. & Svanberg, S. Versatile mobile lidar system for environmental monitoring. *Appl. Opt.* **42,** 3583–3594 (2003).
7. Gol'tsman, G. N. *et al.* Picosecond superconducting single-photon optical detector. *Appl. Phys. Lett.* **79,** 705–707 (2001).
8. Natarajan, C. M., Tanner, M. G. & Hadfield, R. H. Superconducting nanowire single-photon detectors: physics and applications. *Supercond. Sci. Technol.* **25,** 063001 (2012).
9. Correa, R. E. *et al.* Single photon counting from individual nanocrystals in the infrared. *Nano Lett.* **12,** 2953–2958 (2012).
10. Toth, L. E. *Transition Metal Carbides and Nitrides* Ch. 7 (Academic Press, 1971).
11. Marsili, F. *et al.* High quality superconducting NbN thin films on GaAs. *Supercond. Sci. Technol.* **22,** 095013 (2009).
12. Kerman, A. J. *et al.* Constriction-limited detection efficiency of superconducting nanowire single-photon detectors. *Appl. Phys. Lett.* **90,** 101110 (2007).
13. Marsili, F. *et al.* Single-photon detectors based on ultra-narrow superconducting nanowires. *Nano Lett.* **11,** 2048–2053 (2011).
14. Baek, B., Lita, A. E., Verma, V. & Nam, S. W. Superconducting $a$-$W_xSi_{1-x}$ nanowire single-photon detector with saturated internal quantum efficiency from visible to 1850 nm. *Appl. Phys. Lett.* **98,** 251105 (2011).
15. Semenov, A. D., Gol'tsman, G. N. & Korneev, A. A. Quantum detection by current carrying superconducting film. *Physica C* **351,** 349–356 (2001).
16. Bulaevskii, L. N., Graf, M. J. & Kogan, V. G. Vortex-assisted photon counts and their magnetic field dependence in single-photon superconducting detectors. *Phys. Rev. B* **85,** 014505 (2012).
17. Miller, A. J. *et al.* Compact cryogenic self-aligning fiber-to-detector coupling with losses below one percent. *Opt. Express* **19,** 9102–9110 (2011).
18. Lita, A. E., Miller, A. J. & Nam, S. W. Counting near-infrared single-photons with 95% efficiency. *Opt. Express* **16,** 3032–3040 (2008).
19. Lamas-Linares, A. *et al.* in *Proceedings of the Quantum Electronics and Laser Science Conference* QTu3E.1 (Optical Society of America, 2012).
20. Anant, V. *et al.* Optical properties of superconducting nanowire single-photon detectors. *Opt. Express* **16,** 10750–10761 (2008).
21. Yamashita, T. *et al.* Origin of intrinsic dark count in superconducting nanowire single-photon detectors. *Appl. Phys. Lett.* **99,** 161105 (2011).
22. Dorenbos, S. N. *et al.* Superconducting single photon detectors with minimized polarization dependence. *Appl. Phys. Lett.* **93,** 161102 (2008).
23. Semenov, A. *et al.* Optical and transport properties of ultrathin NbN films and nanostructures. *Phys. Rev. B* **80,** 054510 (2009).
24. Driessen, E. F. C. *et al.* Impedance model for the polarization-dependent optical absorption of superconducting single-photon detectors. *Eur. Phys. J. Appl. Phys.* **47,** 10701 (2009).
25. Ekin, J. W. *Experimental Techniques for Low-Temperature Measurements: Cryostat Design, Material Properties, and Superconductor Critical-Current Testing* (Oxford Univ. Press, 2007).
26. Stern, J. A. & Farr, W. H. Fabrication and characterization of superconducting NbN nanowire single photon detectors. *IEEE Trans. Appl. Supercond.* **17,** 306–309 (2007).
27. Kerman, A. J. *et al.* Kinetic-inductance-limited reset time of superconducting nanowire photon counters. *Appl. Phys. Lett.* **88,** 111116 (2006).
28. Ejrnaes, M. *et al.* A cascade switching superconducting single photon detector. *Appl. Phys. Lett.* **91,** 262509 (2007).
29. Marsili, F., Najafi, F., Dauler, E., Molnar, R. J. & Berggren, K. K. Afterpulsing and instability in superconducting nanowire avalanche photodetectors. *Appl. Phys. Lett.* **100,** 112601 (2012).
30. Marsili, F. *et al.* Efficient single photon detection from 500 nanometer to 5 micron wavelength. *Nano Lett.* **12,** 4799–4804 (2012).

## Acknowledgements

The authors thank R. M. Briggs, S. D. Dyer, W. H. Farr, J. Gao, M. Green, E. Grossman, P. D. Hale, R. W. Leonhardt, I. Levin and R. E. Muller for technical support, and S. Bradley, B. Calkins, A. Migdall and M. Stevens for scientific discussions. Part of this work was supported by the Defense Advanced Research Projects Agency (Information in a Photon programme). Part of this research was carried out at the Jet Propulsion Laboratory, California Institute of Technology, under a contract with the National Aeronautics and Space Administration.

## Author contributions

F.M., V.B.V., J.A.S., A.E.L., B.B., R.P.M. and S.W.N. conceived and designed the experiments. F.M., V.B.V., J.A.S., S.H. and T.G. performed the experiments. F.M. and S.H. analysed the data. J.A.S., I.V., M.D.S. and S.W.N. contributed materials/analysis tools. F.M. wrote the paper.

## Additional information

Supplementary information is available in the online version of the paper. Reprints and permissions information is available online at www.nature.com/reprints. Correspondence and requests for materials should be addressed to F.M. and S.W.N.

## Competing financial interests

The authors declare no competing financial interests.